ROYAL SOCIETY
OF CHEMISTRY

COMMUNICATION

Check for updates

Bio-derived ionic coacervate-engineered cellulose liquid crystal films for electrically reconfigurable microwave absorption

Haoyuan Li,[a] Yongjuan Wang,[a] Zhonghui Li,[a] Shuang Liang, [iD][a] Yuming Zhou,[a] Wenhua Gao [iD][b] and Man He [iD]*[a]

The increasing demand for sustainable and intelligent electronics calls for microwave absorption (MA) materials that are simultaneously renewable, mechanically compliant, and electrically reconfigurable—capabilities rarely achieved in current systems dominated by rigid and static absorbers. Here, we introduced a new design strategy that leveraged an ionic coacervate-engineered cellulose liquid crystal film (CLCF) to realize fully reversible, low-voltage, and structurally governed modulation of MA performance. The CLCF integrated a cholesteric cellulose nanocrystal (CNC) scaffold with a poly(ionic liquid) (PIL)/ionic liquid (IL) coacervate network, in which mobile ions, electrostatic interactions, and chiral helical ordering operated cooperatively. This hierarchical architecture preserved long-range cholesteric ordering while introducing ion-transport pathways and heterogeneous interfaces, enabling pronounced field-induced helical reorganization and synergistic conductive, dipolar, and interfacial polarization losses. As a result, the film exhibited voltage-dependent tuning in minimum reflection loss (RL_{min}), peak-frequency position, and effective absorption bandwidth (EAB). At 0 V, the CLCF displayed an RL_{min} of -41.74 dB at 11.5 GHz and an EAB of 2.96 GHz; increasing the voltage to 16 V triggered a low-frequency absorption peak and enhanced the performance to an RL_{min} of -49.02 dB at 8.4 GHz with an EAB of 4.0 GHz, fully covering the X-band. Meanwhile, the incorporation of PIL effectively mitigated the inherent brittleness of CNC assemblies, yielding a flexible, biodegradable, and processable film platform. This work establishes a sustainable and mechanistically distinct route for constructing electrically reconfigurable electromagnetic materials, offering a transferable strategy for next-generation adaptive and eco-friendly electronic systems.

New concepts

This work introduces a conceptually new strategy for constructing electrically reconfigurable microwave-absorbing materials by integrating cholesteric ordering with ionic coacervate nanoarchitectures on a fully bio-derived and flexible platform. We demonstrate that unlike conventional absorbers whose electromagnetic properties are fixed after fabrication, cellulose liquid crystals can serve as an electrically addressable helical scaffold capable of dynamically modulating dielectric anisotropy. The central conceptual advance lies in the ionic coacervate-engineered CNC/PIL/IL framework, wherein mobile ions, electrostatically coordinated polymer chains, and chiral CNC helices engage in multilevel cooperative interactions. This integrated architecture establishes a previously unexplored mechanism in which field-induced helical reorganization synchronizes with voltage-driven ion transport, thereby actively reconfiguring conductive, interfacial, and dipolar polarization losses. Such synergistic reconfiguration generates a highly responsive dielectric system capable of reversible, low-voltage tailoring of absorption intensity, resonance frequency, and effective bandwidth. By uniting sustainability, structural hierarchy, and real-time electromagnetic tunability, this work defines a new design paradigm for intelligent, green, and adaptive microwave absorbers, overcoming long-standing limitations of brittleness, non-renewability, and static performance in existing systems.

1. Introduction

The rapid expansion of communication technologies and the widespread adoption of intelligent and flexible electronic devices have intensified concerns regarding electromagnetic interference and environmental electromagnetic pollution.[1,2] Considerable efforts have therefore been devoted to developing microwave absorption (MA) materials with strong attenuation capability and broad effective bandwidths.[3,4] In parallel, rising global attention to sustainability has stimulated an urgent demand for bio-derived, environmentally benign, and degradable electromagnetic protection materials.[5] However, most high-performance absorbers rely on non-renewable precursors and exhibit structurally fixed absorption characteristics once fabricated, preventing them from adapting to the dynamically evolving electromagnetic environments encountered in modern

[a] *Jiangsu Optoelectronic Functional Materials and Engineering Laboratory, School of Chemistry and Chemical Engineering, Southeast University, Nanjing 211189, China. E-mail: heman@seu.edu.cn*

[b] *State Key Laboratory of Advanced Papermaking and Paper-based Materials, South China University of Technology, Guangzhou 510640, China*

electronics. Smart and flexible devices require real-time, multi-band, and reversible MA modulation, yet conventional absorbers—typically rigid and structurally fixed after fabrication—lack the ability to dynamically tune their dielectric properties and accommodate mechanical deformation.[6,7] Developing intelligent and sustainable MA materials that unify dynamically tunable absorption properties with mechanical flexibility therefore remains a critical unresolved challenge.

Stimuli-responsive MA materials offer a promising route to address this limitation, enabling dynamic modulation of electromagnetic parameters under mechanical, thermal, moisture, or electrical stimuli.[8–10] Among these strategies, electric-field regulation is particularly attractive due to its rapid response, facile operation, and excellent reversibility.[11] However, electrically tunable absorbers that are simultaneously flexible, environmentally sustainable, and highly responsive under low voltages are exceedingly rare, reflecting a fundamental gap in materials design.

Bio-derived liquid crystal materials represent an emerging opportunity for next-generation adaptive electromagnetic platforms.[12] Their intrinsic anisotropy confers strong electric-field responsiveness, allowing reversible reorientation of ordered domains and tunable dielectric permittivity.[13,14] Cellulose nanocrystals (CNCs), in particular, form well-defined chiral nematic (cholesteric) architectures through spontaneous self-assembly, offering a sustainable route to ordered, anisotropic, and biodegradable functional materials.[15,16] Electric fields can modulate CNC helical orientation and pitch, directly influencing interfacial and dipolar polarization processes and establishing a structure–property basis for tunable MA.[17] However, pristine CNC films are intrinsically brittle, and the incorporation of functional components often disrupts cholesteric ordering—highlighting a key material paradox: enhancing tunability typically compromises structural integrity or self-assembly fidelity.[18] To reconcile these competing demands, we introduce poly(ionic liquid) (PIL) and ionic liquid (IL) as cooperative components capable of simultaneously enhancing flexibility and electrical responsiveness. PIL chains electrostatically associate with CNCs to form an interconnected network that mitigates brittleness while preserving the cholesteric framework.[19] Meanwhile, IL introduces mobile ions that enable field-driven charge transport and interfacial polarization, amplifying dielectric reconfigurability. These synergistic effects establish a multi-level coupling between ionic mobility, polymer coordination, and cholesteric organization—an opportunity that remains largely unexplored in the context of intelligent MA systems. Distinct from conventional electrically tunable microwave absorbers that rely on conductivity switching, rigid metasurface resonances, or semiconductor carrier injection, this work realizes electrical tunability through dynamic reconfiguration of polarization processes within a soft, self-assembled cellulose liquid crystal matrix.

Guided by these principles, we report a bio-derived ionic coacervate-engineered cellulose liquid crystal film (CLCF) that integrates sustainability, mechanical flexibility, and electrically tailored MA performance. In this system, negatively charged CNC helices electrostatically crosslink with cationic PIL chains

to form a robust cholesteric scaffold infiltrated with IL. This design preserves the cholesteric order of CNCs while incorporating electrically responsive and flexible components. Under applied voltage, the CNC helices reorient, modulating dielectric anisotropy and widening ion-transport channels to facilitate ion migration and conductive losses. Moreover, the formation of heterogeneous interfaces between mobile ions and the CNC–PIL framework generates strong interfacial polarization, while field-induced dipole alignment enhances dipolar polarization. These cooperative effects result in pronounced enhancement of absorption intensity and a tunable effective absorption bandwidth (EAB) that can be expanded to fully cover the X-band, exhibiting reversible and voltage-controlled behavior. Simultaneously, the PIL network dramatically improves the flexibility and structural integrity of the film. Overall, this work establishes a mechanistically distinct and fully sustainable design paradigm for electrically reconfigurable microwave absorbers, advancing the development of intelligent, flexible, and eco-friendly electromagnetic protection systems for next-generation electronics.

2. Results and discussion

2.1. Structural design and characterization of the CLCF

The CLCF was synthesized *via* a one-pot, two-step ionic coacervation strategy, as illustrated in Fig. 1a. In this process, high-aspect-ratio, negatively charged CNCs (Fig. S1) were sequentially mixed with PIL and IL, inducing spontaneous ionic coacervation through strong electrostatic attraction between the cationic PIL and anionic CNC surfaces. The PIL, bearing imidazolium cations, was synthesized *via* epoxide ring-opening polymerization of epichlorohydrin (ECH) followed by quaternization (Fig. S2). The resulting PIL compound was characterized by proton nuclear magnetic resonance (^{1}H NMR) spectra, carbon nuclear magnetic resonance (^{13}C NMR) spectra and X-ray photoelectron spectroscopy (XPS) (Fig. S3–S8).[20,21] Notably, both PIL and IL share the same chloride anion and imidazolium cation, which minimizes ionic incompatibility during coacervation. The abundant positive charges on PIL chains promote dense electrostatic association with CNCs, triggering dynamic self-assembly of nanofibers into interconnected bundles *via* a synergistic mechanism of noncovalent bonding and chain entanglement. These bundles constitute the skeleton of the cholesteric liquid crystal film, while the inter-bundle voids form nanoconfined ion-transport channels.[22] Meanwhile, the flexible PIL chains mitigate the intrinsic brittleness of rigid CNCs, improving the mechanical flexibility and toughness of the coacervate network without compromising its structural order.[23] Subsequent infiltration of IL into the CNC/PIL coacervate framework further enhances ion mobility and facilitates long-range ionic conduction through percolative ion-transport pathways. Overall, this coacervate-driven assembly locks CNCs into an ordered cholesteric arrangement while integrating ionic functionality and mechanical compliance—both essential for voltage-tunable MA.
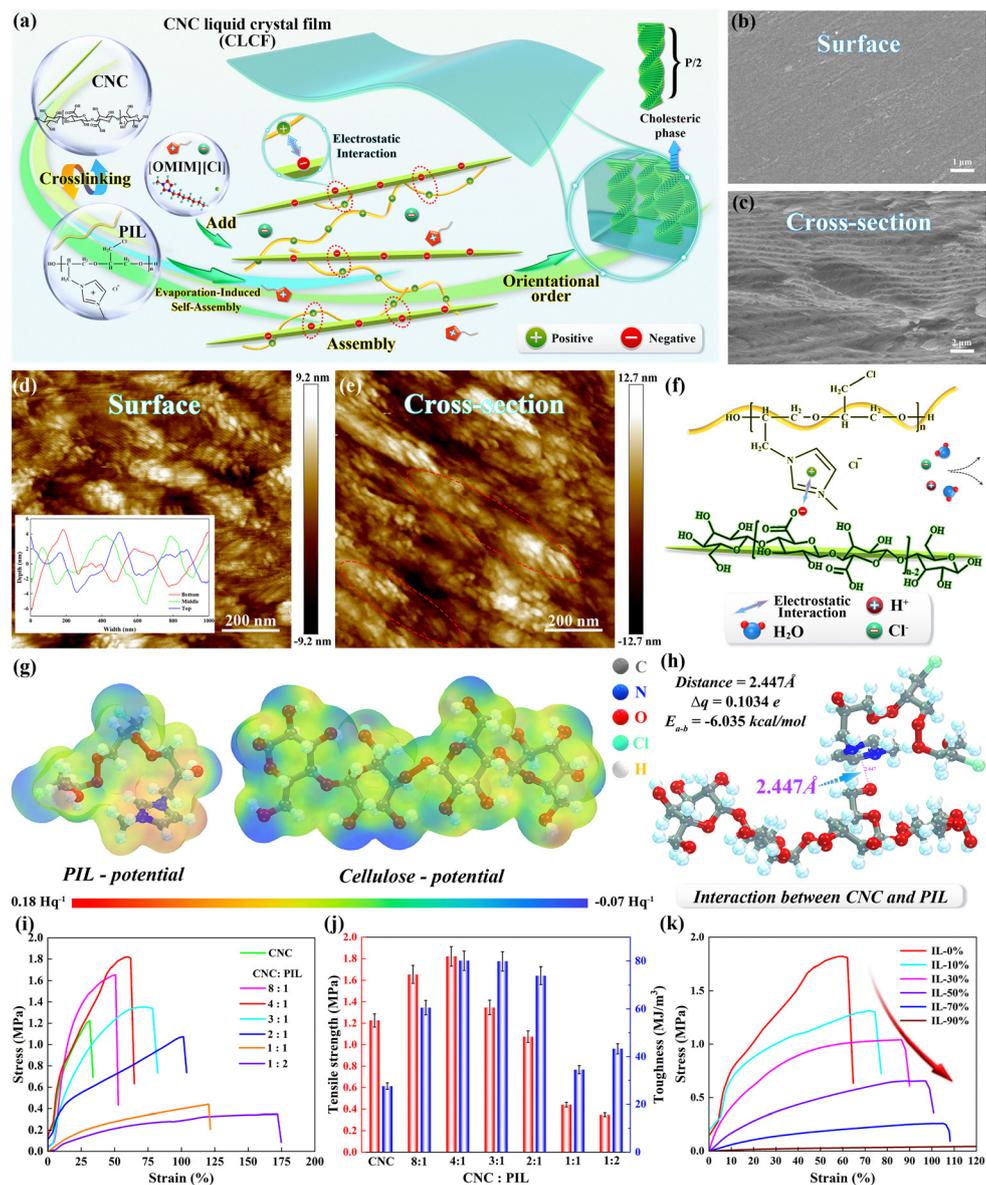
Fig. 1 Synthesis and characterization of the CLCF. (a) Schematic illustration of the synthesis process. SEM images of the CLCF (b) surface and (c) cross-section. AFM images of the CLCF (d) surface and (e) cross-section. (f) Schematic illustration of the interactions between the CNC and PIL. (g) The calculated ESP maps of the CNC and PIL. (h) The binding energy and molecular distance between the CNC and PIL. (i) Tensile stress–strain curves and (j) strength and toughness of the CNC and CNC–PIL films. (k) Tensile stress–strain curves of the CLCF with varying IL fractions.

Fourier transform infrared (FT-IR) spectroscopy confirmed the incorporation of PIL and IL into the CNC framework (Fig. S9). The characteristic aromatic C–H stretching vibration appeared in the CLCF, verifying the presence of imidazolium cations. After adding PIL, the shape of the O–H stretching band is broadened and the center of the peak is red shifted (from 3287 cm^{-1} to 3331 cm^{-1}). The red shift and pronounced broadening of the O–H stretching band originate from strengthened and diversified hydrogen-bonding interactions, which weaken the O–H bond and generate a distribution of vibrational environments due to the coexistence of hydrogen bonds with varying strengths and configurations. X-ray diffraction (XRD) analysis (Fig. S10) further corroborated the structural evolution during fabrication. The CNC

exhibited a typical cellulose I crystalline phase, and addition of PIL does not alter this crystalline structure, suggesting minimal disruption of CNC domains. Upon IL incorporation, partial disruption of CNC hydrogen bonding interactions facilitates IL penetration into the crystalline regions, leading to an increased interlayer spacing as reflected by a slight (200) peak shift.[24]

The morphology and microstructure of the dried CLCF were characterized using scanning electron microscopy (SEM) and atomic force microscopy (AFM). As shown in Fig. 1b and c, the surface of the CLCF exhibited a smooth and uniform morphology, while the cross-section revealed a well-defined Bouligand structure, characteristic of helicoidal CNC arrangements. Elemental mapping (Fig. S11) showed higher concentrations of Cl

and N within the cross-section, suggesting that IL preferentially infiltrates the interior of the cholesteric framework during assembly. AFM analysis further revealed nanoscale wavy textures on the surface and helical arrangements in the cross-section (Fig. 1d and e), confirming the preservation of cholesteric ordering. The successful construction of the CLCF skeleton is ensured by strong electrostatic interactions and hydrogen bonding between the negatively charged hydroxyl groups of the CNC and the positively charged imidazolium moieties of PIL, as validated by density functional theory (DFT) calculations (Fig. 1f–h and Fig. S12–S15).[25] Electrostatic potential (ESP) maps were obtained to visualize the spatial distribution of electron density in the CNC and PIL (Fig. 1g and Fig. S12–S15).[26] The blue regions, representing electron-rich oxygen atoms on the CNC, are poised to interact with the red regions corresponding to the electron-deficient imidazole rings on PIL. These complementary regions facilitate noncovalent complexation during the evaporation-induced self-assembly process. The optimized complex exhibited a binding distance of 2.447 Å between the oxygen atom of the CNC and the centroid of the imidazole ring, with a binding energy of -6.035 kcal mol^{-1} and an electron transfer of 0.1034e (Fig. 1h), confirming strong noncovalent interactions that drive coacervate self-assembly. Experimental results from zeta potential and water contact angle measurements (Fig. S16 and S17) further supported these findings, demonstrating progressive surface charge neutralization and enhanced hydrophobicity upon PIL incorporation—indicative of robust electrostatic and hydrogen-bonding interactions within the coacervate network.

To further correlate molecular interactions with macroscopic mechanical performance, tensile stress–strain measurements were conducted on CNC–PIL composite films with varying CNC : PIL mass ratios (Fig. 1i and j). The CNC acts as a rigid nanofibrillar scaffold, while PIL functions as a flexible, ductile polymer binder. With increasing PIL content, both tensile strength and toughness exhibited a nonmonotonic trend—rising to a maximum at a moderate PIL loading and subsequently decreasing. The optimal mechanical performance was achieved at a CNC : PIL mass ratio of 4 : 1, with the tensile strength and toughness fracture strain of the material reaching 1.83 MPa and 80.15 MJ m^{-3}, where a balanced interplay between rigidity and flexibility enabled efficient stress transfer. This behavior arises from coacervation-driven associative assembly at moderate PIL levels, which promotes denser nanofiber packing and more efficient stress transfer.[27] In contrast, excessive PIL results in a soft polymer-dominant phase with reduced structural integrity and stiffness, resembling the mechanical response of ductile polymeric networks. Polarized optical microscopy (POM) observations (Fig. S18 and S19) confirmed that the CNC–PIL composite films maintained the characteristic cholesteric liquid crystalline texture, indicating that PIL incorporation does not disrupt the intrinsic helical order of the CNC. The effect of IL content on the mechanical properties of the CLCF was further investigated (Fig. 1k). The tensile strength of the CLCF decreased monotonically with increasing IL content, primarily due to IL infiltration into CNC crystalline domains that disrupts intermolecular

interactions within the coacervate network, thereby compromising mechanical integrity.[28,29] Even at an IL loading of 50 wt%, the CLCF retained its well-defined cholesteric ordering (Fig. S20) and satisfactory mechanical robustness, exhibiting a tensile strength of 0.76 MPa and a fracture strain of 100.8%. In contrast to conventional polymer-based flexible MA composites (Fig. S21), the bio-derived CLCF achieves superior elongation at break, underscoring the potential of sustainable materials to rival or even surpass synthetic systems in flexibility. The observed mechanical robustness is design-driven, arising from the synergistic combination of rigid CNC scaffolds, ductile PIL binders, and a controlled IL content that plasticizes the network while preserving the cholesteric framework. The mechanical robustness and structural integrity of the CLCF ensure a reliable framework for voltage-driven modulation of its electromagnetic absorption behavior.

2.2. Correlation of ionic conduction–polarization coupling with microwave absorption in the CLCF

Given that all constituents of the CLCF are intrinsically nonmagnetic, the MA performance is determined exclusively by the complex permittivity (ε' and ε''). The ε' represents the dielectric storage capability of the material, whereas ε'' reflects the dielectric loss responsible for converting electromagnetic energy into heat. As shown in Fig. 2a and b, both ε' and ε'' values of the CLCFs increased markedly with rising IL content, where ε' rose from 2.01 to 7.51 and ε'' from 0.13 to 2.86. This enhancement primarily stems from the improved ionic conductivity induced by IL incorporation. Correspondingly, the dielectric loss tangent ($\tan \delta_\varepsilon = \varepsilon''/\varepsilon'$), indicative of the overall dielectric dissipation capability, exhibited a monotonic increase with increasing IL loading (Fig. 2c), confirming the strengthened dielectric loss ability. To further elucidate the correlation between dielectric behavior and ion transport dynamics, the electrochemical characteristics of CLCFs with varying IL contents were systematically examined. Both the open-circuit voltage (V_{OC}) (Fig. 2d) and ionic conductivity (Fig. S22) initially increased with increasing IL fraction and then slightly declined at higher IL loadings, reflecting the balance between the enhanced availability of mobile ions and the disruption of ordered ion-transport pathways at high IL loadings.[30] It should be noted that the V_{OC} does not directly quantify ionic conductivity; rather, it reflects ion redistribution and interfacial charge accumulation under equilibrium conditions. In contrast, ionic conductivity characterizes bulk ion transport under an applied electric field, and the combined analysis of V_{OC} and conductivity therefore provides complementary insight into interfacial polarization and charge transport within the gel. Electrochemical impedance spectroscopy (EIS) further revealed a progressive reduction in the semicircular radius of the Nyquist plots with increasing IL content (Fig. 2e), implying decreased charge-transfer resistance (R_{ct}) and enhanced carrier mobility, as corroborated by direct resistance measurements (Fig. S23).[25,31] These results collectively confirm that IL incorporation effectively promotes ion mobility and charge accumulation within the CNC–PIL coacervate network, thereby establishing a robust ionic conduction
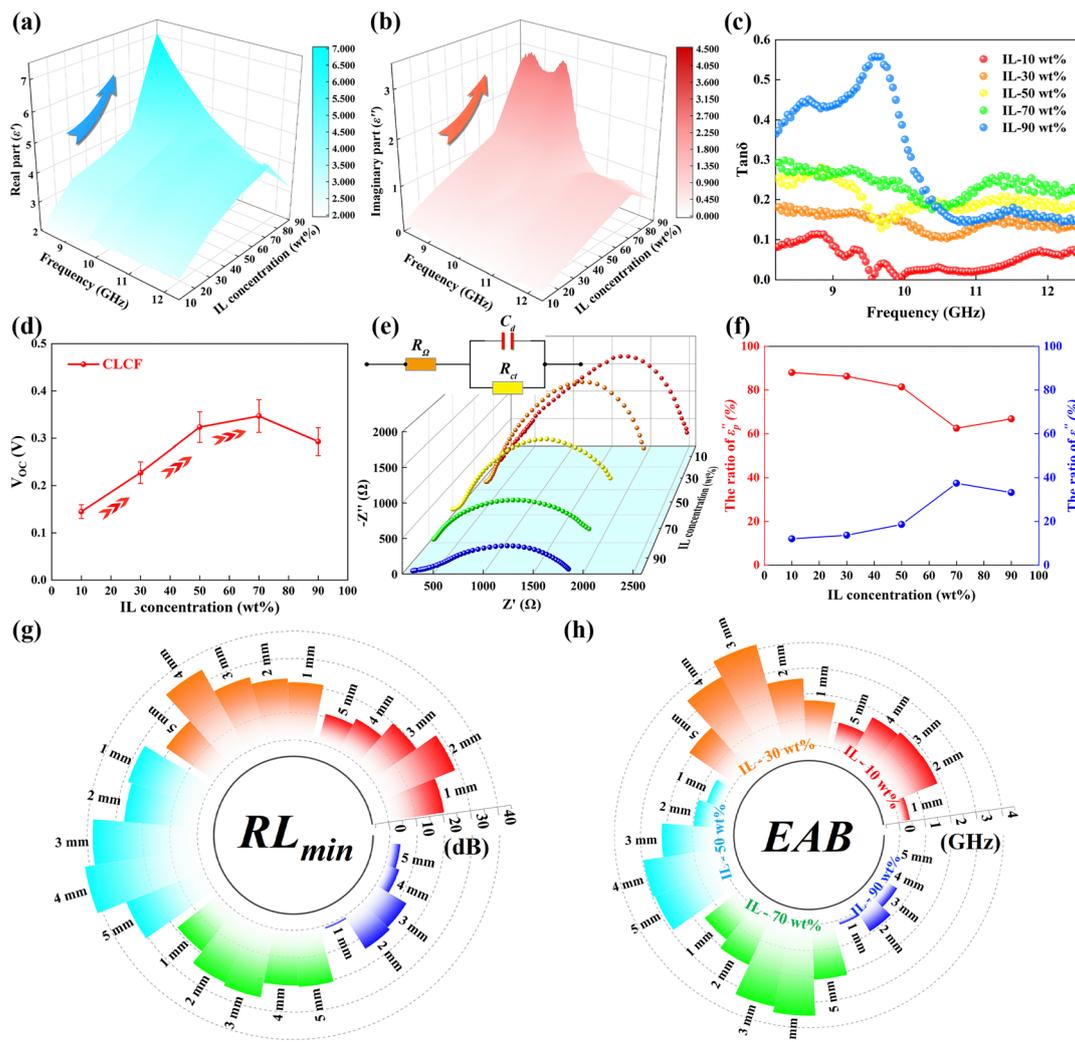
Fig. 2 MA performance analysis of the CLCF with varying IL weight fractions. (a) ε', (b) ε'' and (c) $\tan\delta_\varepsilon$ curves of the CLCF. (d) Open-circuit voltage V_{OC} of the CLCF. (e) EIS of the CLCF. Inset: Equivalent circuit model. (f) Average ε''_c and ε''_p ratios of the CLCF. (g) RL_{min} and (h) EAB values of the CLCF.

framework that underpins the enhanced dielectric response of the CLCF. This is attributed to the high concentration of IL infiltrating and disrupting the hydrogen-bonding network, which facilitates the extension of conductive pathways. Meanwhile, the increased number of ions interacting with the CNC–PIL coacervate network generates richer heterogeneous interfaces, thereby enhancing interfacial polarization. To gain deeper insight into the respective roles of conduction and polarization processes in dielectric loss, the conductive (ε''_c) and polarization (ε''_p) loss components were quantitatively evaluated (see the SI for computational details).[32] As shown in Fig. 2f, with increasing IL content, ε''_c progressively increased while ε''_p correspondingly decreased; however, ε''_p remained the dominant contributor to dielectric loss, indicating that polarization relaxation still played a major role in microwave attenuation. This conclusion was further supported by the Cole–Cole plots (Fig. S24), where each sample exhibits a semicircular shape and each semicircle represents a single relaxation process. This relaxation arises

from interfacial polarization induced by charge inhomogeneity at the interfaces between the CNC as the low-conductivity phase and IL as the ion-enriched phase, which dominates the overall polarization loss. Notably, as the IL content increased, a red shift of the relaxation peak was observed. This shift can be attributed to the fact that the increase in IL content induces microphase separation, which sharpens the electrical contrast between the two phases. Accumulated charges at the interfaces then take longer to dissipate or neutralize along tortuous paths, slowing down the overall relaxation process.[33]

To further investigate the MA performance of the CLCFs, the minimum reflection loss (RL_{min}) and EAB were calculated based on the transmission line theory (see the SI for details).[34,35] As shown in Fig. 2g, h and Fig. S25, the statistical results of RL_{min} and EAB exhibited a non-monotonic dependence on the IL content—first increasing and then decreasing with rising IL fraction. This trend arises from the balance between dielectric loss and impedance matching. Increasing the IL content enhances both conductive and polarization loss,

thereby augmenting the overall dielectric dissipation. However, excessive IL disrupts impedance matching due to high ionic conductivity, resulting in stronger reflection and weaker absorption of incident microwaves. Among all samples, the CLCF containing 50 wt% IL exhibited the optimal MA performance, which originates from a balanced synergy between impedance matching and attenuation capability—two complementary and indispensable factors for efficient absorption. As shown in Fig. S26 and S27, the attenuation coefficient (α) increased monotonically with IL loading, whereas the normalized input impedance (Z_{in}/Z_0) of the 50 wt% IL sample was closest to 1, indicating ideal impedance matching.[36] Thus, the superior MA performance of the 50 wt% IL film resulted from the optimal combination of energy dissipation

and impedance matching, enabling efficient attenuation of incident electromagnetic waves.

2.3. Voltage-driven dielectric response and tunable microwave absorption mechanism in the CLCF

To further explore the voltage-dependent tunability of electromagnetic properties in the CLCF, the modulation of complex permittivity across the X-band was systematically investigated. The activation voltage (V_a, 6 V) corresponds to the onset of a pronounced increase in permittivity, while the saturation voltage (V_s, 16 V) marks the point where permittivity reaches its maximum. As shown in Fig. 3a–c, once V_a was reached, both ε' and ε'' increased markedly across the entire X-band. Upon

Fig. 3 Regulation of the MA performance of the CLCF under external voltage. (a) ε', (b) ε'' and (c) tan δ_ε curves of the CLCF in normal, activated, and saturated states. Cole–Cole curves of the CLCF in (d) normal, (e) activated, and (f) saturated states. (g) ε_c'' and ε_p'' of the CLCF in normal, activated, and saturated states. (h) Evolution of RL and EAB values of the CLCF in normal, activated, and saturated states (under the same 3.8 mm thickness). 3D RL plots of the CLCF in (i) normal, (j) activated, and (k) saturated states.

further increasing the voltage to V_s, ε'' continued to rise due to intensified IL migration, leading to greater dielectric energy dissipation. Consistently, the dielectric loss tangent (tan $\delta_\varepsilon = \varepsilon''/\varepsilon'$) corroborated the enhanced dielectric dissipation capability of the CLCF under external electric fields. The voltage-induced evolution of permittivity primarily arises from two cooperative mechanisms: partial reorganization of the cholesteric helical structure, which alters the anisotropic dielectric environment,[37] and voltage-driven directional migration of IL molecules, which amplifies conductive loss and polarization effects. To elucidate their respective contributions, the conductive $\left(\varepsilon_c''\right)$ and polarization $\left(\varepsilon_p''\right)$ loss components were quantitatively analyzed. As shown in Fig. 3g and Fig. S28, both ε_c'' and ε_p'' exhibited an overall increasing trend with rising voltage, consistent with the elevation of ε''. This behavior reveals that the applied electric field promotes structural and interfacial evolution within the composite. Specifically, the cholesteric CNC domains tend to reorient along the field direction, and the helical structure partially unwinds into a macroscopically nematic-like phase. Such structural reorganization broadens ion-transport channels and facilitates IL migration, thereby enhancing ionic conduction and conductive loss. Meanwhile, the formation of heterogeneous interfaces between IL cations and the CNC–PIL network induces strong interfacial polarization, while field-induced dipole alignment further enhances dipolar polarization. Notably, ε_p'' remains dominant across all voltage states, reflecting the synergistic contribution of abundant surface functional groups and robust interfacial polarization at the IL/CNC–PIL interfaces. Further insights into these relaxation processes were obtained from the Cole–Cole plots (Fig. 3d–f), which exhibited multiple depressed arcs and an oblique tail under elevated voltages. Under saturated bias, although no pronounced relaxation peaks are observed in the frequency-dependent dielectric spectra, the distorted semicircles in the Cole–Cole plots indicate distributed polarization relaxation with non-Debye characteristics.[38] The emergence of additional arcs and the enhanced linear region signify intensified interfacial/dipolar polarization and conductive loss, respectively.[39] This voltage-induced modulation of relaxation behavior confirms that the tunable dielectric response of the CLCF originates from dynamic structural rearrangements and enhanced charge carrier dynamics. Collectively, these coupled effects endow the CLCF with electrically tunable impedance and loss characteristics, enabling dynamic control of both absorption intensity and frequency position.

These variations in permittivity directly impact the MA performance of the CLCF. As shown in the 3D and two-dimensional (2D) RL maps (Fig. 3h–k and Fig. S29), with increasing voltage, the RL_{min} value deepened from -41.74 dB at 11.5 GHz (0 V) to -43.61 dB at 9.7 GHz (V_a) and further to -49.02 dB at 8.4 GHz (V_s), indicating enhanced attenuation capability and low-frequency shift of the absorption peak (Fig. 3h–k). Simultaneously, the EAB exhibited an apparent expansion and frequency shift. At zero bias, the CLCF achieved an EAB of 2.96 GHz (from 9.44 to 12.4 GHz) at a thickness of 4.4 mm, covering approximately 70.5% of the X-band. Upon applying increasing

voltage, the EAB extended and migrated in frequency, reaching 4.2 GHz (8.2–12.4 GHz) at 2.5 mm and 4.0 GHz (8.2–12.2 GHz) at 3.8 mm, ultimately achieving the full X-band coverage (Fig. S29). Notably, RL_{min} shifted toward lower frequencies with increasing voltage, indicating a voltage-responsive frequency-selective absorption behavior. This voltage-induced enhancement in MA performance stems from synergistic improvements in impedance matching and dielectric loss.[40,41] The calculated impedance ratio $|Z_{in}/Z_0|$ (Fig. S30) progressively approached the ideal range of 0.8–1.2 as the voltage increased, facilitating efficient coupling of incident electromagnetic waves into the absorber. Meanwhile, the attenuation constant α (Fig. S31) increased significantly under voltage stimulation, particularly in the low-frequency region, signifying enhanced electromagnetic energy dissipation. These effects can be attributed to the field-driven reorganization of the cholesteric ordered structure and directional migration of IL molecules, which together enhance conductive loss and strengthen interfacial and dipolar polarization. The resultant reconfiguration of the internal chiral architecture not only extends the conductive network but also modulates charge storage and dynamic polarization behavior across frequencies.[42–44] Collectively, these coupled effects endow the CLCF with electrically tunable impedance and loss characteristics, enabling dynamic modulation of both absorption intensity and frequency band—paving the way for intelligent, adaptive microwave absorbers. In addition, cyclic switching between 0 and 16 V (Fig. S32) demonstrated excellent reversibility and stability of the voltage modulation, with negligible changes in both RL_{min} and EAB, confirming the robustness of the dynamic tuning process. This reversibility originates from the elastic restoring force of the cholesteric CNC scaffold and the dynamically cross-linked CNC–PIL–IL network, which enables field-induced structural reorganization and ion redistribution without permanent structural degradation.

The electromagnetic absorption mechanism of the CLCF is schematically illustrated in Fig. 4, based on the above discussions. The overall attenuation behavior arises from the synergistic contributions of conductive and polarization losses, both modulated by voltage-driven structural evolution and ion migration. For clarity, the absorption process was categorized into two states: "No electric field" and "Voltage-driven regulation".

2.3.1. No electric field. In the absence of an external bias, the CLCF maintains its cholesteric liquid crystalline phase, where the CNC/PIL framework, interspersed with conductive IL, establishes interconnected ion-transport pathways that facilitate effective impedance matching. This favorable matching condition enables efficient coupling of the incident electromagnetic wave (EMW) into the absorber. Conductive loss primarily originates from the motion of mobile ions under the alternating electromagnetic field, leading to ohmic dissipation. In addition, the abundant polar functional groups (*e.g.*, C–O and C–N) induce dipolar polarization, while interfacial polarization is reinforced by charge heterogeneity at the CNC/PIL/IL interfaces, leading to localized space-charge accumulation. These synergistic effects collectively endow the CLCF with strong intrinsic MA capability under zero bias.

2.3.2. Voltage-driven regulation. Upon application of an external electric field, CNC nanorods—acting as dielectric
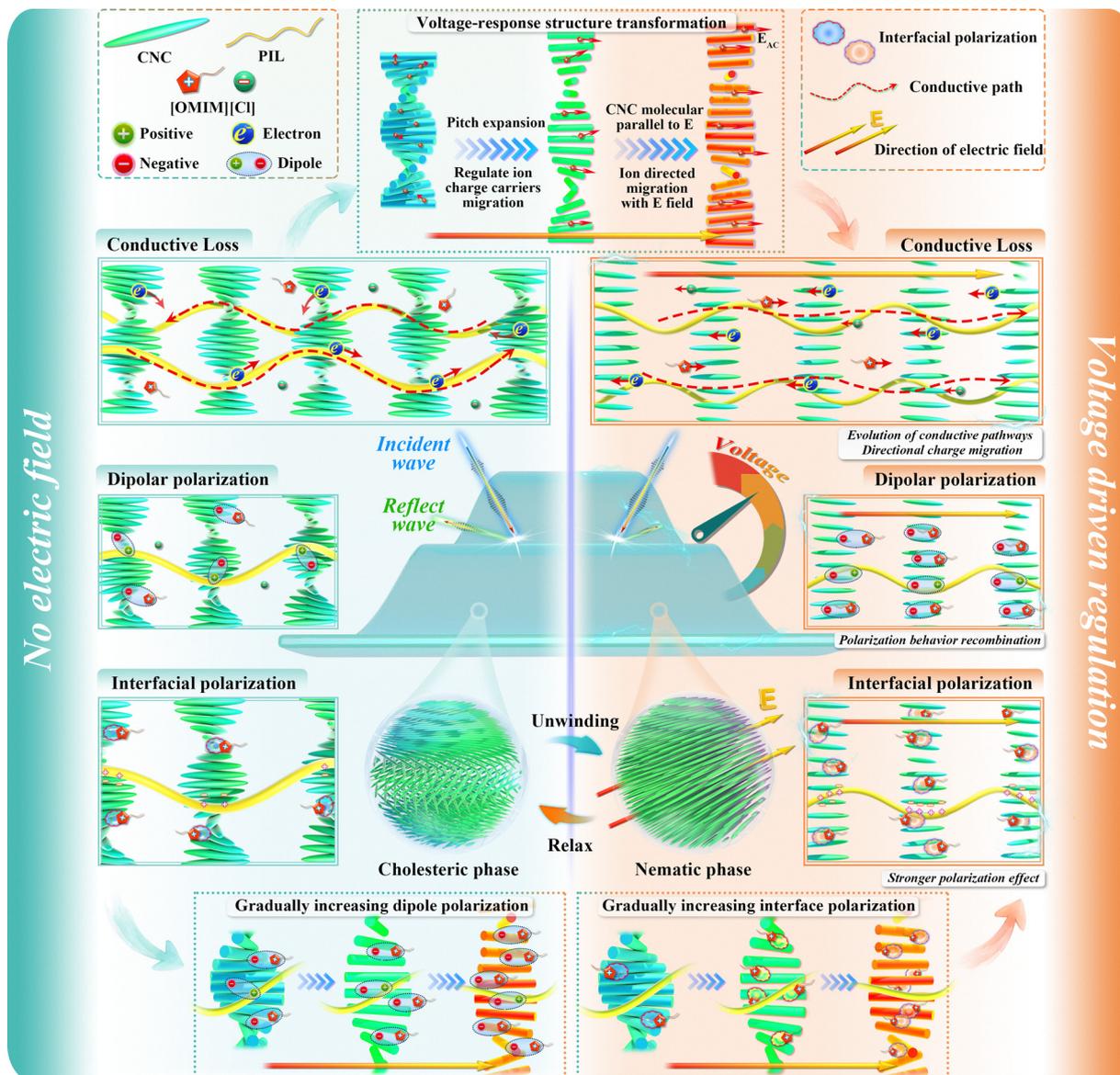
Fig. 4 Schematic diagram of the tunable wave absorption mechanism for the CLCF.

anisotropic units—experience an electrostatic torque that partially unwinds the cholesteric helix toward a nematic-like alignment. Notably, this voltage-driven helical reorganization establishes a direct structure–dielectric coupling, wherein partial unwinding of the cholesteric architecture simultaneously facilitates ion migration and intensifies interfacial and dipolar polarization, thereby enhancing the dielectric response. POM observations confirmed this transformation (Fig. S33), revealing a pronounced reorientation of cholesteric domains along the field direction and thereby inducing a transition from helical to macroscopically nematic order. This structural evolution widens the ion-transport channels and increases the available free volume for ion motion,[45,46] which facilitates directional migration of IL ions and thereby enhances ionic conduction and conductive loss. As evidenced by the Nyquist plots (Fig. S34), the semicircular radius progressively decreased with increasing

voltage, indicating reduced charge-transfer resistance and enhanced carrier mobility. Meanwhile, increased IL penetration into the CNC–PIL framework generates additional heterogeneous interfaces, giving rise to pronounced interfacial polarization. In parallel, the field-induced alignment of molecular dipoles further strengthens dipolar polarization. These cooperative effects—synergistic enhancement of conductive, interfacial, and dipolar polarization losses—constitute the fundamental mechanism underlying the dynamically tunable MA performance of the CLCF under voltage stimuli.

2.4. RCS simulation of the CLCF

In order to assess the far-field EMW response of the CLCF during voltage-driven transition, radar cross-section (RCS) was conducted using the Computer Simulation Technology (CST) software (Fig. 5).[47] RCS quantifies the intensity of EMW scattered by a

target under radar illumination and serves as a critical parameter for evaluating electromagnetic detectability and stealth performance. By simulating RCS profiles under different voltage states, valuable insights into the dynamic electromagnetic wave–target interactions and the tunable stealth capability of the CLCF were obtained. The simulation model consists of a dual-layer square structure (Fig. 5a), comprising a perfectly electrically conducting (PEC) substrate and an upper CLCF layer. In this context, a reduced RCS signifies lower electromagnetic wave reflection and enhanced stealth capability. As shown in the 3D RCS simulations (Fig. 5d), the PEC-only sample exhibits the strongest reflected signal intensity, underscoring its poor performance in stealth

applications. In contrast, substantial attenuation of the RCS signal is observed upon the introduction of the CLCF, particularly under applied voltages. As illustrated in Fig. 5b and c, the RCS values of CLCF-coated structures remain consistently below 0 dB across a broad angular range (−100° to 100°), in stark contrast to the PEC baseline. Moreover, as the applied voltage increases, the RCS value of the CLCF coating further decreases. This notable suppression of scattered signals aligns well with the experimentally observed enhancement in MA performance, validating the voltage-tunable stealth functionality of the CLCF system.

To further elucidate the underlying dielectric loss mechanisms of the CLCF under external electric fields, simulations of
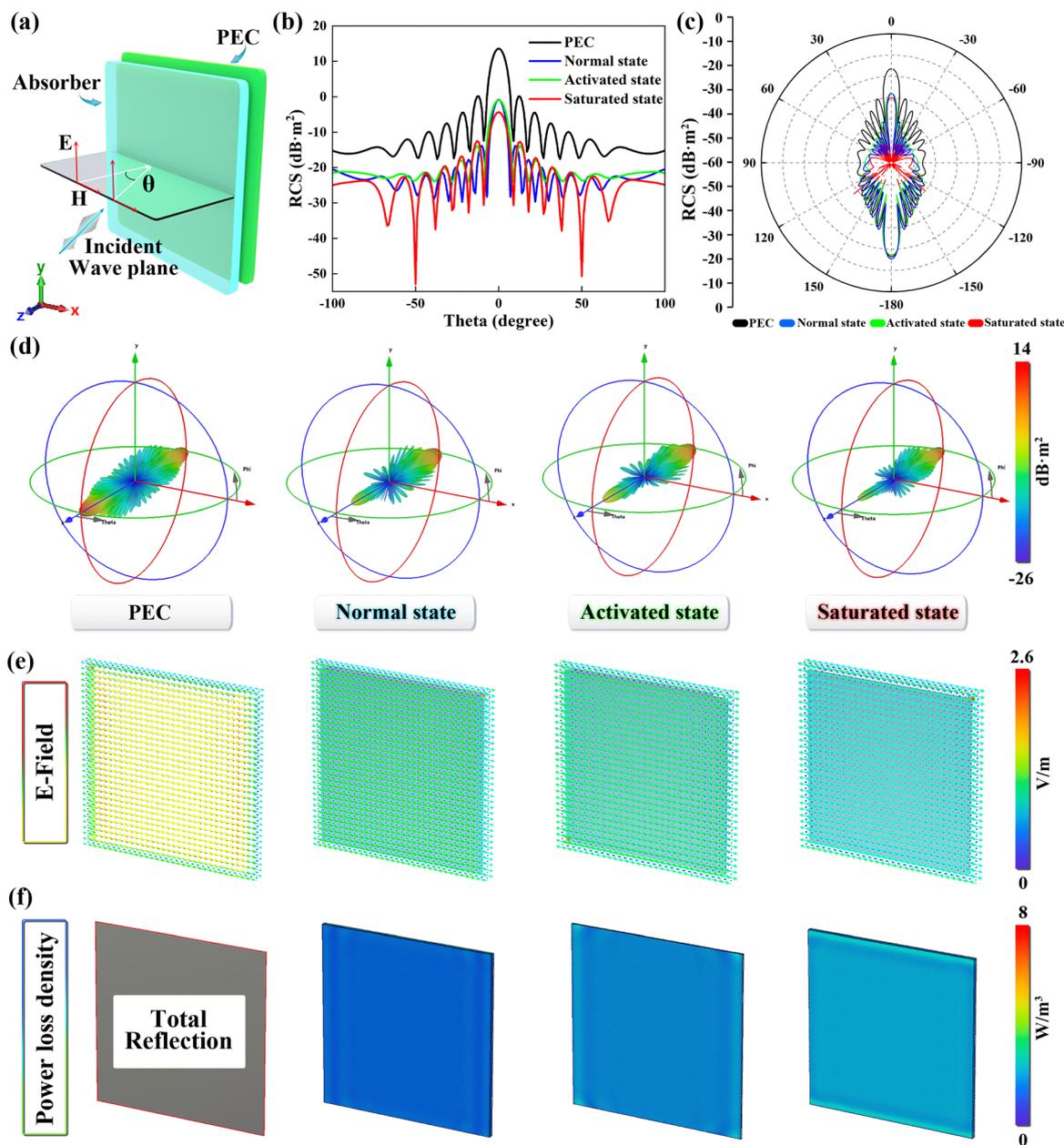

Fig. 5 Simulation and theoretical calculations. (a) CST model. (b) RCS simulated values of a PEC substrate and the CLCF in different states within the scanning angle range from −100° to 100°. (c) RCS signal values in all directions. (d) 3D plots of the RCS signal value, (e) the induced current field and (f) the power loss density of the samples with different voltages.

surface electric field distribution and power loss density were conducted across different voltage states.[48] As shown in Fig. 5e, the electric field intensity on the surface of a bare PEC substrate is significantly higher than that of the CLCF-covered structures, as indicated by the color gradient. Upon applying voltage, a progressive attenuation in the electric field intensity within the CLCF layer is observed, as shown by the reduced surface field contrast. This attenuation reflects improved impedance matching, which reduces the generation of reflected (counter-radiating) electromagnetic fields at the interface. As a result, a greater portion of the incident EMW is able to penetrate into the absorber rather than being reflected. This inference is further supported by the power loss distribution maps shown in Fig. 5f. Under increasing voltage, the CLCF layer exhibited an increase in power loss density, particularly within the bulk of the material, indicating enhanced dielectric energy dissipation. The voltage-driven evolution of the internal cholesteric structure and intensified ion migration synergistically enhance polarization and conductive loss, thereby facilitating stronger dielectric response and more efficient conversion of electromagnetic energy into heat.[8,49] These findings underscore the tunable and efficient EMW attenuation capability of the CLCF system.

3. Conclusions

In summary, an intelligent and sustainable ionic coacervate-engineered CLCF was developed, featuring a cholesteric CNC/PIL framework infiltrated with IL, which achieved reversible and electrically tailored MA alongside outstanding mechanical flexibility. The synergistic incorporation of PIL and IL enhanced both intrinsic absorption capability and voltage responsiveness. Under applied voltage, field-induced helical reorganization of CNCs and synergistic conductive and interfacial/dipolar polarization losses generated a strong dielectric response, enabling efficient and reversible modulation of MA performance. With increasing voltage, the absorption intensity strengthened, the absorption peak shifted toward lower frequencies, and the EAB broadened. At 0 V, the CLCF showed an RL_{min} of -41.74 dB at 11.5 GHz and an EAB of 2.96 GHz ($\sim$70.5% of the X-band); at 16 V, the RL_{min} improved to -49.02 dB at 8.4 GHz with an EAB of 4.0 GHz, fully covering the X-band. In addition, PIL effectively mitigated the inherent brittleness of CNC films, endowing the CLCF with outstanding flexibility and robustness, as evidenced by a tensile strength of 0.76 MPa and an elongation at break of 100.8%. This work presents a renewable, environmentally benign strategy for electrically reconfigurable microwave absorbers and establishes a versatile platform for intelligent, flexible, and green electromagnetic protection technologies.

4. Experimental section

Comprehensive details of the experimental design are provided in the SI.

Author contributions

Haoyuan Li: methodology, conceptualization, data curation, visualization, formal analysis, and writing – original draft. Yongjuan Wang: data curation. Zhonghui Li: investigation and data curation. Yuming Zhou: supervision and funding acquisitions. Shuang Liang: supervision and writing – review & editing. Wenhua Gao: funding acquisitions and writing – review. Man He: conceptualization, writing – review & editing, project administration, supervision, and funding acquisitions.

Conflicts of interest

There are no conflicts to declare.

Data availability

The data that support the findings of this study are available from the corresponding author upon reasonable request.

Supplementary information (SI) is available. See DOI: https://doi.org/10.1039/d5mh02357b.

Acknowledgements

References

1 X. Wang, F. You, Q. Yao, K. Wang, Y. Liao, G. Tong, X. Wang, T. Wu and W. Wu, *Mater. Horiz.*, 2023, **10**, 2677–2690.

2 M. He, W. Qian, H. Li, Z. Li, H. Chen, Y. Zhou, X. Bu and Y. Wang, *Chem. Eng. J.*, 2025, **506**, 159777.

3 F. You, X. Liu, M. Ying, Y. Yang, Y. Ke, Y. Shen, G. Tong and W. Wu, *Mater. Horiz.*, 2023, **10**, 4609–4625.

4 K. Fu, Q. Yao, L. Xu, W. Zhou, Z. Wang, Y. Yang, G. Tong, X. Wang and W. Wu, *Mater. Horiz.*, 2024, **11**, 1065–1078.

5 D. Wang, T. Ping, Z. Du, X. Liu and Y. Zhang, *Nano-Micro Lett.*, 2024, **17**, 100.

6 M. Zhang, Q. Zheng, W.-Q. Cao and M.-S. Cao, *Mater. Horiz.*, 2025, **12**, 1440–1451.

7 X. Yan, H. Zhao, F. Liu, C. Yu, X. Jiang and J. Guo, *Mater. Horiz.*, 2026, DOI: 10.1039/d5mh01919b.

8 P. Chen, S. He, Z. Zou, T. Wang, J. Hu, J. Tao, L. Yang and Y. Li, *Adv. Funct. Mater.*, 2025, 2506308.

9 Z. Y. Wang, Z. C. Li, B. Li, A. F. Shi, L. Zhang, Y. B. Zhu, F. Ye and S. H. Yu, *Adv. Mater.*, 2024, **36**, 2412605.

10 M. He, X. Lv, Z. Li, H. Li, W. Qian, S. Zhu, Y. Zhou, Y. Wang and X. Bu, *Small*, 2024, **20**, 2403210.

11 H. Lv, Z. Yang, H. Xu, L. Wang and R. Wu, *Adv. Funct. Mater.*, 2019, **30**, 1907251.

12 G. Chu, *Acc. Mater. Res.*, 2024, **5**, 1388–1400.

13 X. Zhang, L. Li, Y. Chen, C. Valenzuela, Y. Liu, Y. Yang, Y. Feng, L. Wang and W. Feng, *Angew. Chem., Int. Ed.*, 2024, **63**, e202404202.

14 J. Hobbs, C. J. Gibb and R. J. Mandle, *Nat. Commun.*, 2025, **16**, 7510.

15 F. Zhang, J. Yu, W. Zhong, Z. Wang, Q. Li and G. Qing, *ACS Nano*, 2025, **19**, 6299–6308.

16 M. Goyal, C. Shi, M. Hassanpour, J. Xu, X. Zhuang, X. Song, A. Y. Song and Z. Zhang, *Adv. Colloid Interface Sci.*, 2026, **347**, 103688.

17 S. Ghosh, E. Abraham and I. I. Smalyukh, *ACS Nano*, 2023, **17**, 19767–19778.

18 M. Xu, Z. Xu, M. A. Soto, Y. T. Xu, W. Y. Hamad and M. J. MacLachlan, *Adv. Mater.*, 2023, **35**, 2301060.

19 Q. Wang, W. Niu, S. Feng, J. Liu, H. Liu and Q. Zhu, *ACS Nano*, 2023, **17**, 14283–14308.

20 X. Li, D. Lv, L. Ai, X. Wang, X. Xu, M. Qiang, G. Huang and X. Yao, *ACS Nano*, 2024, **18**, 12970–12980.

21 S.-Y. Zhang, Q. Zhuang, M. Zhang, H. Wang, Z. Gao, J.-K. Sun and J. Yuan, *Chem. Soc. Rev.*, 2020, **49**, 1726–1755.

22 W. Chen, T. Dong, Y. Xiang, Y. Qian, X. Zhao, W. Xin, X. Y. Kong, L. Jiang and L. Wen, *Adv. Mater.*, 2021, **34**, 2108410.

23 H. Wang, A. Gupta, Q. Lu, W. Wu, X. Wang, X. Huang, X. Hu and P. S. Lee, *Nat. Commun.*, 2025, **16**, 7405.

24 H. Jiang, R. Bai, Y. Zhao, S. Shi, G. Jiang and D. Zhao, *Adv. Funct. Mater.*, 2025, 2503512.

25 X. Li, X. Wang, M. Li, W. Zhu, H. Luo, X. Lu, H. Xu, J. Xue, F. Ye, H. Wu and X. Fan, *Adv. Funct. Mater.*, 2024, **35**, 2407217.

26 X. Kou, Y. Huang and Y. Yang, *J. Hazard. Mater.*, 2021, **420**, 126623.

27 Q. Li, S. Zheng, Z. Liu, W. Li, X. Wang, Q. Cao and F. Yan, *Adv. Mater.*, 2024, **36**, 2413901.

28 C. Shan, M. Che, A. Cholewinski, R. Su and B. Zhao, *Cell Rep. Phys. Sci.*, 2023, **4**, 101511.

29 Z. Xu, B. Zhu, X. Liu, T. Lan, Y. Huang, Y. Zhang and D. Wu, *Chem. Eng. J.*, 2023, **477**, 147246.

30 H. Lee, A. Erwin, M. L. Buxton, M. Kim, A. V. Stryutsky, V. V. Shevchenko, A. P. Sokolov and V. V. Tsukruk, *Adv. Funct. Mater.*, 2021, **31**, 2103083.

31 H. Lv, Y. Yao, M. Yuan, G. Chen, Y. Wang, L. Rao, S. Li, U. I. Kara, R. L. Dupont, C. Zhang, B. Chen, B. Liu, X. Zhou, R. Wu, S. Adera, R. Che, X. Zhang and X. Wang, *Nat. Commun.*, 2024, **15**, 1295.

32 R. Hu, J. Luo, H. Wen, C. Liu, J. Peng, Z. Xiong, D. Wang, Z. Feng, Y. Peng and R. Che, *Adv. Funct. Mater.*, 2024, **35**, 2418304.

33 Y. Liang, L. Deng, B. Luo, L. Zhang, K. Tao, X. Li, Q. Chen and H. Wu, *iScience*, 2025, **28**, 112366.

34 L. Duan, J. Zhou, Y. Yan, J. Tao, Y. Liu, Y. Lei, K. Zou, Y. Wang, H. Huang, X. Tao, P. Liu, Y. Ma and Z. Yao, *Adv. Funct. Mater.*, 2024, **35**, 2416727.

35 M. He, X. Lv, H. Peng, Y. Zhou, H. Li, Z. Li, Y. Wang and X. Bu, *Chem. Eng. J.*, 2024, **491**, 151726.

36 M. He, H. Chen, H. Peng, Y. Zhou, Z. Song, Y. Wang, S. Feng and X. Bu, *Chem. Eng. J.*, 2023, **456**, 140985.

37 P. Oliwa, P. Kapuściński, M. Popławska, M. Muszyński, M. Król, P. Morawiak, R. Mazur, W. Piecek, P. Kula, W. Bardyszewski, B. Piętka, H. Sigurðsson and J. Szczytko, *Adv. Sci.*, 2025, **12**, 2500060.

38 J. Wen, Y. Liu, S. Hui, L. Deng, L. Zhang, X. Fan, Q. Chen, X. Liu, X. Li, N. Yan and H. Wu, *Matter*, 2025, **8**, 102151.

39 J. Wang, L. Zhang, J. Yan, J. Yun, W. Zhao, K. Dai, H. Wang and Y. Sun, *Adv. Funct. Mater.*, 2024, **34**, 2402419.

40 M. Samet, V. Levchenko, G. Boiteux, G. Seytre, A. Kallel and A. Serghei, *J. Chem. Phys.*, 2015, **142**, 194703.

41 M. Samet, A. Kallel and A. Serghei, *J. Compos. Mater.*, 2022, **56**, 3197–3217.

42 C. Zhang, G. Chen, K. Zhang, B. Jin, Q. Zhao and T. Xie, *Adv. Mater.*, 2024, **36**, 2313078.

43 R. Zhang, Z. Song, W. Cao, G. Gao, L. Yang, Y. He, J. Han, Z. Zhang, T. Wang and J. Zhu, *Light: Sci. Appl.*, 2024, **13**, 223.

44 S. Hui, Q. Chen, K. Tao, L. Zhang, X. Fan, R. Che and H. Wu, *Adv. Mater.*, 2024, **37**, 2415844.

45 D. Qu and E. Zussman, *J. Phys. Chem. Lett.*, 2020, **11**, 6697–6703.

46 D. Qu and E. Zussman, *Adv. Opt. Mater.*, 2022, **10**, 2101659.

47 H. Long, Y. Qian, S. Gang, W. Zhang, B. Yang, Y. Wei, B. Wang, W. Li and Q. Jiang, *ACS Nano*, 2025, **19**, 1819–1831.

48 X. Liu, W. Ma, T. Yang, Z. Qiu, J. Wang, Y. Li, Y. Wang and Y. Huang, *ACS Nano*, 2024, **18**, 10184–10195.

49 X. Liu, L. Wu, J. Liu, H. Lv, P. Mou, S. Shi, L. Yu, G. Wan and G. Wang, *Carbon Energy*, 2024, **6**, e589.